

# Combined Experimental and Theoretical Study of Acetylene Semi-Hydrogenation over Pd/Al<sub>2</sub>O<sub>3</sub>

Liliana P. L. Gonçalves,<sup>a,b</sup> Jianguang Wang,<sup>c</sup> Simone Vinati,<sup>d</sup> Emanuele Barborini,<sup>d</sup> Xian-Kui Wei,<sup>e</sup> Marc Heggen,<sup>e</sup> Miguel Franco,<sup>a</sup> Juliana P. S. Sousa,<sup>a</sup> Dmitri Y. Petrovykh,<sup>a</sup> Olívia Salomé G. P. Soares,<sup>b</sup> Kirill Kovnir,<sup>f,g</sup> Jaakko Akola,<sup>c,h,\*</sup>, Yury V. Kolen'ko<sup>a,\*</sup>

<sup>a</sup> International Iberian Nanotechnology Laboratory (INL), Avenida Mestre José Veiga, 4715-330 Braga, Portugal;

E-mail: [yury.kolenko@inl.int](mailto:yury.kolenko@inl.int)

<sup>b</sup> Laboratory of Separation and Reaction Engineering - Laboratory of Catalysis and Materials (LSRE-LCM), Faculdade de Engenharia, Universidade do Porto, Rua Dr. Roberto Frias, 4200-465 Porto, Portugal

<sup>c</sup> Computational Physics Laboratory, Tampere University, P.O. Box 692, 33014 Tampere, Finland;

E-mail: [jaakko.akola@ntnu.no](mailto:jaakko.akola@ntnu.no)

<sup>d</sup> Tethis S.p.A., Milan 20143, Italy

<sup>e</sup> Ernst Ruska-Centre for Microscopy and Spectroscopy with Electrons and Peter Grünberg Institute, Forschungszentrum Jülich GmbH, 52425 Jülich, Germany

<sup>f</sup> Department of Chemistry, Iowa State University, Ames, Iowa 50011, United States

<sup>g</sup> Ames Laboratory, U.S. Department of Energy, Ames, Iowa 50011, United States

<sup>h</sup> Department of Physics, Norwegian University of Science and Technology, 7491 Trondheim, Norway

## Abstract

The semi-hydrogenation of acetylene ( $\text{C}_2\text{H}_2 + \text{H}_2 = \text{C}_2\text{H}_4$ ,  $\Delta H = -172 \text{ kJ mol}^{-1}$ ) is a well-studied reaction that is important for purification of ethylene,  $\text{C}_2\text{H}_4$ , feed used in polyethylene production. Pd-based catalysts are most commonly used to remove acetylene from ethylene feed prior to Ziegler-Natta polymerization because acetylene is a poison for Ziegler-Natta catalysts. New applications of the analogous catalytic processes, with similar requirements on the conversion and selectivity, are considered for the storage of  $\text{H}_2$  within the context of the  $\text{H}_2$  economy. Here, a combination of experimental and theoretical studies was employed to explore the performance of synthesized Pd nanoparticles and the feasibility of using computational modelling for predicting their catalytic properties. Specifically, a model 5%Pd/Al<sub>2</sub>O<sub>3</sub> nanocatalyst was successfully synthesized using high-throughput flame spray pyrolysis (FSP) method. As a catalyst for acetylene semi-hydrogenation, the material shows high conversion of 97%, a modest selectivity of 62%, and a turnover frequency of ethylene formation of  $5 \text{ s}^{-1}$ . The experimental data were further supported by computational modelling of catalytic properties. Results of microkinetic simulations, based on parameters obtained from DFT calculations, over a Pd<sub>30</sub>/Al<sub>2</sub>O<sub>3</sub>(100) model system were correlated with experiments. The insights from this direct comparison of theory and experiments provide indications for future improvements of the theoretical predictions and for novel types of materials with improved catalytic properties.

## Keywords

Heterogeneous catalysis, Hydrogenation, Kinetics, DFT, Modelling, Nanoclusters.

## 1. Introduction

An important industrial example of the semi-hydrogenation of acetylene,  $C_2H_2$ , to ethylene,  $C_2H_4$  ( $C_2H_2 + H_2 = C_2H_4$ ), is related to the need to reduce to a few ppm the acetylene concentration in the ethylene feedstock for polyethylene polymerization, which is typically produced from steam cracking of hydrocarbons and contains 0.5–2% of acetylene [1]. Without the catalytic semi-hydrogenation, this minor amount of acetylene negatively affects the polymerization process because acetylene poisons the polymerization Ziegler-Natta catalysts. Furthermore, to keep the process economically viable, the catalyst should not further convert ethylene into ethane, meaning that highly selective semi-hydrogenation of acetylene needs to be achieved [2,3]. Similar needs for improving the selectivity of catalysts [4] also emerges from the recent advances in the  $H_2$  economy, whereby catalytic hydrogenation of unsaturated hydrocarbons, such as cyclohexane, methylcyclohexane, decalin, etc. [5] offers a promising pathway to store/use renewable  $H_2$ .

Pd-based catalysts have been employed in semi-hydrogenation of  $C_2H_2$  to  $C_2H_4$  due to their high activity for acetylene conversion. Unfortunately, these catalysts typically exhibit low selectivity because they subsequently convert  $C_2H_4$  to unwanted  $C_2H_6$  [6–8]. They also present limited stability caused by the accumulation of oligomers, which is mostly attributed to the fact that these catalysts provide active sites that enable side reactions [9–11]. An increase in the selectivity and stability of Pd catalysts has been achieved by, for example, the addition of promoters to the catalysts, or by mixing with other metals and metal oxides [12–17]. Despite the numerous studies addressing the improvement of Pd-based catalysts, it is still not possible to increase their selectivity and stability, a goal that requires understanding the catalytic reaction mechanism.

The reaction pathways of acetylene hydrogenation on Pd(111) surface have been investigated using first-principles DFT calculations, and the results revealed that the hydrogenation of acetylene to vinyl and vinyl to ethylene had similar activation barriers [18]. Later, using first-principles-based kinetic Monte Carlo simulations, Me *et al.* reported that the simulated apparent activation energy, ethylene selectivity and reaction orders were comparable with experiments [19]. More recently, semi-hydrogenation of acetylene over Pd-doped Cu(111) surfaces at low-temperature has been examined by DFT combined with microkinetic modeling [20]. It was found that the ethylene selectivity on a single-Pd-doped Cu(111) surface was higher than that of a monolayer-Pd-doped Cu(111), but the acetylene conversion exhibited inverse behaviors on these two surfaces. Until now, most theoretical studies have focused on the hydrogenation of acetylene over metal surfaces, while the investigations of Pd anchored on a supporting material remain a considerable challenge [21,22]. Accordingly, to develop advanced catalysts for semi-

hydrogenation of  $C_2H_2$ , it is necessary to achieve a basic understanding of the catalytic reactions on model systems.

Herein, we report new synthesis, characterization, and catalytic hydrogenation properties of a Pd nanocatalyst supported on alumina, **Pd/Al<sub>2</sub>O<sub>3</sub>**. Moreover, we investigate whether a state-of-the-art theoretical modeling can predict the catalytic behavior. The results of this study show a good agreement between the performed experiments and theoretical simulations, which opens a practical opportunity for computational screening of complex catalysts.

## 2. Experimental

### 2.1 Catalyst preparation

The flame spray pyrolysis (FSP) sample was produced employing a commercial FSP system (NPS10, Tethis, Italy). The NPS10 is a bench top system that allows the production of FSP nanopowder with laboratory mass-scale for R&D purposes. The burner where the pyrolysis reactions take place is described, for example, by Mädler *et al* [23]. In our work, a liquid solution containing the metal organometallic precursors was injected, by a syringe pump (at a rate of  $5\text{ cm}^3\text{ min}^{-1}$ ) through a stainless-steel capillary, into a nozzle where it was dispersed by an oxygen flow of  $5\text{ dm}^3\text{ min}^{-1}$  (at a pressure drop of 1.5 bar). A concentric flamelet ring was fed with a premixed mixture of methane/oxygen ( $CH_4\ 1.5\text{ dm}^3\text{ min}^{-1}$ ,  $O_2\ 3.2\text{ dm}^3\text{ min}^{-1}$ ) for generating the supporting flame. Additional oxygen ( $5\text{ dm}^3\text{ min}^{-1}$ ) was supplied by an outer sheath flow to assure enough oxidant for complete conversion of the reactants. The powder was collected on a glassfiber filter (GF/A Whatman, Kent, United Kingdom), 150 mm in diameter. The filter was placed in a water-cooled holder 400 mm above the nozzle.

The liquid precursor was prepared by dissolving Pd(II)-acetylacetonate (99% Strem Chemicals) into acetonitrile (anhydrous, 99.8%, Sigma Aldrich) and then placing a suitable quantity of the obtained solution into a premixed solution of Al(III)-*sec*-butoxide (98%, Strem Chemicals) and Xylene (Carlo Erba) in order to form a final solution of 0.69 M of Al. This synthesized sample will be referred to as **Pd/Al<sub>2</sub>O<sub>3</sub> as-synthesized**. The obtained Pd loading was 5%, matching the loading of the reference commercial catalyst, which has been previously comprehensively characterized [11,24].

### 2.2 Catalyst Characterization

**2.2.1 X-ray diffraction.** Powder X-ray diffraction (XRD) patterns of the samples were obtained using a X'Pert PRO diffractometer (PANalytical) with a PIXcel 3D detector, set at 45 kV and 40 mA. The sample was grounded to a fine powder and placed in the sample holder. A Bragg Brentano configuration was used in a  $2\theta$  range from  $20^\circ$  to  $80^\circ$  with step size of  $0.01^\circ$  and a time

per step of 300 s. Obtained data were analysed with High Score software (PanAnalytical), matching the patterns to International Centre for Diffraction Data (ICDD) database.

**2.2.2 Electron microscopy.** A probe-corrected FEI Titan 80–200 Chemi-STEM microscope, equipped with a high-brightness Schottky field emission electron gun, was operated at 200 kV to carry out the structural and morphological analysis of the as-synthesized catalyst. The scanning transmission electron microscope (STEM) images were collected by a high-angle annular-dark-field (HAADF) detector in an angle range between 70 mrad and 200 mrad.

**2.2.3 X-ray photoelectron spectroscopy.** Supported-catalyst powders were analysed in an ESCALAB 250 Xi system (Thermo Scientific). As-synthesized, oxidized, and reduced samples were scraped onto Al foil substrates and measured using a non-monochromatic Al K $\alpha$  X-ray source (operating at 400 W power) to minimize charging artefacts. Peak fitting was performed in Avantage instrument software (Thermo Scientific), choosing a minimal number of components that produced random residuals consistently for all the samples. A convolution of Gaussian and Lorentzian line shapes was used for most of the spectral components; Pd 3d peaks required small asymmetric tails.

The binding energy (BE) scale is based on a BE shift (uniformly applied for all the samples) that placed the aliphatic C 1s peak associated with the supported-catalyst material to  $285.0 \pm 0.2$  eV, the value chosen based on previous measurements on non-metallic surfaces: polymer films [25], adventitious carbon [26], and alkane chains in self-assembled monolayers [27]. This BE correction places the (unresolved) Al 2p peak associated with the alumina of the catalyst support particles at  $74.6 \pm 0.2$  eV.

Due to the apparent differential charging, there was a consistent (for all the samples) shift of  $2.5 \pm 0.1$  eV between the high-resolution elemental peaks corresponding to the supported-catalyst particles and Al-foil substrate: aliphatic C 1s component as well as aluminum-oxide Al 2p and O 1s components. This differential charging shift enabled an unambiguous selection of the aliphatic C 1s component associated with the supported-catalyst particles to be used as the above-mentioned BE reference.

**2.2.4 Nitrogen physisorption.** The surface area, pore size, and pore volume of the samples were calculated with the determination of the N<sub>2</sub> adsorption-desorption isotherms of the samples at –77 K. The characterization was performed using a Quantachrome Autosorb IQ2 multi-station apparatus. Approximately 100 mg of sample was placed in the sample holder and outgassed under vacuum at 423 K for 240 min before the analysis. The specific surface area of the samples was determined according to the Brunauer–Emmett–Teller (BET) method in the range of ( $0.05 < P/P_0 < 0.3$ ), the pore size was determined by the Barrett–Joyner–Halenda (BJH) method and

the pore volume was determined using the amount of vapor adsorbed at relative pressure close to unity ( $P/P_0 = 0.97$ ).

**2.2.5 Hydrogen Chemisorption.**  $H_2$  chemisorption experiments on the Pd catalysts were performed on an AMI-200 Catalyst Characterization apparatus (Altamira) and using the pulsed method, in which pulses of 58  $\mu\text{L}$  of  $H_2$  are injected in the carrier gas (Ar,  $25\text{ cm}^3\text{ min}^{-1}$ ) that flows through the sample, until the metal saturation, i.e., until the peak area becomes constant. The adsorbed hydrogen quantity is calculated by the integration of each peak that comes from each pulse, determined using a thermal conductivity detector (TCD). Before the analysis, the sample was preheated to 473 K in a pure Ar flow and left for 1 h, next, the flow is exchanged to a pure flow of hydrogen and the sample is reduced for 1 h. After the reduction, the system was purged with Argon and cooled down to 308 K. The hydrogen adsorption stoichiometry was assumed to be 0.5  $H_2$ :Pd [28].

### 2.3 Catalytic measurements on acetylene semi-hydrogenation reaction

Catalytic measurements were performed in a continuous-flow fixed-bed quartz reactor with internal diameter of 7 mm, using quartz wool to trap the catalyst inside the reactor. The temperature in the bed was measured using a Type K thermocouple connected to a thermocouple data logger, and the gases, acetylene (2.6), hydrogen (5.0) and helium (5.0), were supplied using Bronkhorst mass flow controllers. The reaction products were analysed by a GC-2010 Plus from Shimadzu, equipped with a VP-Alumina column and a flame ionization detector (FID). The reactor was loaded with 1 mg of catalyst diluted in 100 mg silicon carbide (SiC) (60–80 mesh) and prior to each experiment, the catalyst was reduced *in situ* at 473 K for 30 min, under a  $20\text{ cm}^3\text{ min}^{-1}$   $H_2$  flow.

The conversion and selectivity of the catalysts were evaluated by isothermal and temperature-programmed experiments at atmospheric pressure for both the prepared sample after reduction (**Pd/Al<sub>2</sub>O<sub>3</sub> reduced**) and a commercial 5%Pd/Al<sub>2</sub>O<sub>3</sub> catalyst (**Pd/Al<sub>2</sub>O<sub>3</sub>\_Ref reduced**) (Alfa Aesar), which was used as reference. In the case of the isothermal experiments at 473 K, after the reduction treatment, the gas flow was changed to a mixture of 2%  $C_2H_2$  and 20%  $H_2$  balanced with helium at a total flow rate of  $50\text{ cm}^3\text{ min}^{-1}$  and the time on stream was 9 h to evaluate the stability of the catalyst. For the temperature-programmed experiments, after reduction, the temperature was reduced to 300 K in  $20\text{ cm}^3\text{ min}^{-1}$  helium flow and then the gas flow was changed to the same composition as in the isothermal experiments. The temperature was increased in 50 K steps at  $10\text{ K min}^{-1}$ . In each step, the composition of the gas flow was analysed after 30 min of stabilization.

The conversion on acetylene ( $X_{C_2H_2}$ ) was calculated using the following equation:

$$X_{C_2H_2}(\%) = \frac{C_2H_2(feed) - C_2H_2}{C_2H_2(feed)} \quad (1)$$

Where  $C_2H_2(feed)$  is the concentration of acetylene on the feed and  $C_2H_2$  is the concentration of acetylene in the product stream. The selectivity in ethylene formation ( $S_{C_2H_4}$ ) was calculated as follows:

$$S_{C_2H_4}(\%) = \frac{C_2H_4}{C_2H_2(feed) - C_2H_2} \quad (2)$$

where  $C_2H_4$  is the concentration of ethylene in the product stream.

The Turnover Frequency ( $TOF$ ) was calculated as:

$$TOF = \frac{\text{No. of } C_2H_4 \text{ molecules formed}}{\text{No. of exposed Pd sites on catalyst} \times \text{time}} \quad (3)$$

The activation energy ( $E_a$ ) for acetylene hydrogenation under the established conditions for the tested samples was calculated from the Arrhenius plot as:

$$E_a = -\text{slope}(\text{Arrhenius plot}) \times R \quad (4)$$

where  $R$  is the gas constant.

## 2.4 Computational modeling details

The structures and energies of the reactant, transition, and product states in acetylene hydrogenation over an alumina-supported Pd cluster were calculated using the density functional theory (DFT) methods as implemented in the CP2K program package [29,30]. All calculations were carried out spin-polarized within the generalized gradient approximation (GGA) using the Perdew, Burke, and Ernzerhof (PBE) exchange-correction potential [31] and analytical pseudopotentials of the type suggested by Goedecker, Teter, and Hutter (GTH) [32]. The Kohn-Sham wave functions were expanded in a double-zeta valence polarized (DZVP) basis set [33] which was optimized based on molecular properties. An auxiliary plane-wave basis with a 600 Ry kinetic energy cutoff was used to describe the electron density of valence electrons [34]. Only the  $\Gamma$ -point was employed for Brillouin zone integration as the model systems are laterally large and the alumina substrate (slab) is an insulator. The DFT-D3 method with the standard parameters suggested by Goerigk and Grimme was employed to correct the dispersion interaction [35]. Bader analysis of effective charges on atoms was used to determine the charge transfer [36,37], and the reaction paths were calculated using the climbing-image nudged elastic band (CI-NEB) method [38].

A periodic slab model was used for the support by cleaving a bulk  $\gamma$ -Al<sub>2</sub>O<sub>3</sub> model [39] in the (100) direction. The Al<sub>2</sub>O<sub>3</sub>(100) support was chosen as a four-layer ( $4 \times 3$ ) slab (in total 480 atoms, lateral size  $22.33 \times 25.19 \text{ \AA}^2$ ) and a vacuum spacing of at least  $24 \text{ \AA}$  thickness in the vertical direction. The top two atomic layers were allowed to relax during the simulations while the bottom two layers were fixed. Here, a Pd<sub>30</sub> cluster with the square-base pyramidal structure was chosen as a representative model catalyst structure. Previously, the same structure with 30 Pd atoms (*fcc*) was used for Pd and Pd–O clusters based on the correspondence with electron microscopy analysis [40]. To justify the Pd<sub>30</sub>/Al<sub>2</sub>O<sub>3</sub> model as a representative choice, a larger model catalyst composed of a pyramidal Pd<sub>55</sub> cluster and an Al<sub>2</sub>O<sub>3</sub>(100) support with (5 x 3)-four-layer-slab (600 atoms, lateral size of  $27.33 \times 25.19 \text{ \AA}^2$ ) has been tested. After optimization, Pd<sub>55</sub> still displays the pyramid-like configuration with a base dimension of  $10.71 \times 10.78 \text{ \AA}^2$ . The nearest distances of cluster images are 16.6 and 14.4  $\text{\AA}$  in lateral directions, large enough to avoid interactions between cluster images, as imposed by periodic boundary conditions. The situation is comparable to the Pd<sub>30</sub>/Al<sub>2</sub>O<sub>3</sub> model where the corresponding image distances are 14.3 and 17.2  $\text{\AA}$ . For these two model structures, our DFT calculations reveal that the differences for acetylene adsorption energy (0.06 eV) and Bader charge on acetylene molecule (0.01 $e$ ) are marginal. Meanwhile, the computational cost of the larger Pd<sub>55</sub>/Al<sub>2</sub>O<sub>3</sub> model is more than an order of magnitude more expensive. Thus, we consider the Pd<sub>30</sub>/Al<sub>2</sub>O<sub>3</sub> model structure both as feasible and representative for reaction modelling. Here, we need to declare that a larger model catalyst would need a much larger substrate to suppress cluster-cluster interactions due to periodic boundary conditions. This would lead to model structures of several thousands of atoms (most of them in the substrate) which is not feasible for DFT simulations in this context.

For acetylene hydrogenation over **Pd<sub>30</sub>/Al<sub>2</sub>O<sub>3</sub>(100)** it was assumed that atomic hydrogen is already available on the catalyst surface (See Supporting Information). Based on the co-adsorption configuration of H\* + H\*, the adsorption sites of C<sub>2</sub>H<sub>2</sub> and C<sub>2</sub>H<sub>4</sub> were optimized by considering different sites on the cluster surface. Here, the adsorption energy ( $E_{ads}^2$ ) was calculated as

$$E_{ads}^2 = E(\text{adsorbate}) + E(\text{Pd}_{30}(\text{H})_2/\text{Al}_2\text{O}_3) - E(\text{adsorbate}(\text{H})_2 + \text{Pd}_{30}/\text{Al}_2\text{O}_3) \quad (5)$$

where  $E(Y)$  is the total energy of the corresponding system  $Y$ .

Microkinetic simulations were performed based on data (parameters) from DFT calculations over the **Pd<sub>30</sub>/Al<sub>2</sub>O<sub>3</sub>(100)** model catalyst to study the acetylene hydrogenation under varying conditions [41–43]. The full details of the microkinetic model have been explained by Ma *et al.* [42]. The simulations were carried out at temperatures from 300 to 500 K, atmospheric pressure

and feed composition of 2% C<sub>2</sub>H<sub>2</sub> and 20% H<sub>2</sub>. The kinetic values were estimated once the simulations were equilibrated to a steady state.

The acetylene conversion ( $X_{C_2H_2}$ ) and ethylene formation selectivity ( $S_{C_2H_4}$ ) were calculated as

$$X_{C_2H_2} = \frac{(R_{C_2H_4} + R_{C_2H_6})}{R_{C_2H_2}} \quad (6)$$

$$S_{C_2H_4} = \frac{R_{C_2H_4}}{(R_{C_2H_4} + R_{C_2H_6})} \quad (7)$$

where  $R$  refers to the reaction rate for the formation of the corresponding species.

### 3. Results

#### 3.1 Characterization results

A 5% Pd on Al<sub>2</sub>O<sub>3</sub> sample (**Pd/Al<sub>2</sub>O<sub>3</sub> as-synthesized**) was prepared by flame spray pyrolysis (FSP), characterized, and tested for acetylene semi-hydrogenation reaction to achieve a basic understanding of the catalytic semi-hydrogenation of acetylene to ethylene on basic model systems. The powder XRD pattern of **Pd/Al<sub>2</sub>O<sub>3</sub> as-synthesized** (Figure 1) shows the characteristic peaks of cubic Al<sub>2</sub>O<sub>3</sub> corresponding to the support, and the presence of PdO is confirmed by the presence of a peak at  $2\theta$  of ca. 34°.

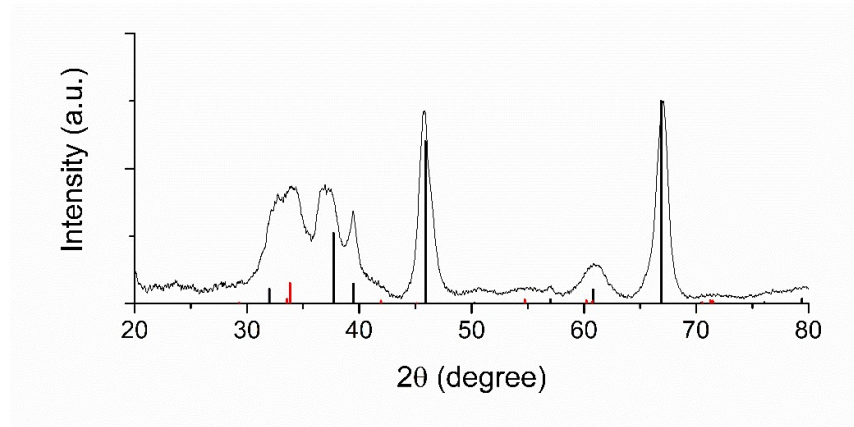


**Figure 1:** XRD pattern of the as-synthesized Pd/Al<sub>2</sub>O<sub>3</sub> catalyst. Red lines: PdO; Black lines: Al<sub>2</sub>O<sub>3</sub>.

By imaging using high-angle annular-dark-field technique in scanning transmission electron microscopy (HAADF–STEM), PdO nanoparticles are observed to be uniformly anchored on the Al<sub>2</sub>O<sub>3</sub> support (Figure 2a). Statistical measurements reveal that sizes of the crystalline PdO particles on the **Pd/Al<sub>2</sub>O<sub>3</sub> as-synthesized** sample are in the 1–5 nm range, and the Al<sub>2</sub>O<sub>3</sub> supports have diameters in the 10–35 nm range. In Figure 2b, close inspection of the morphology reveals that most of the PdO particles have elongated shapes and form agglomerates.



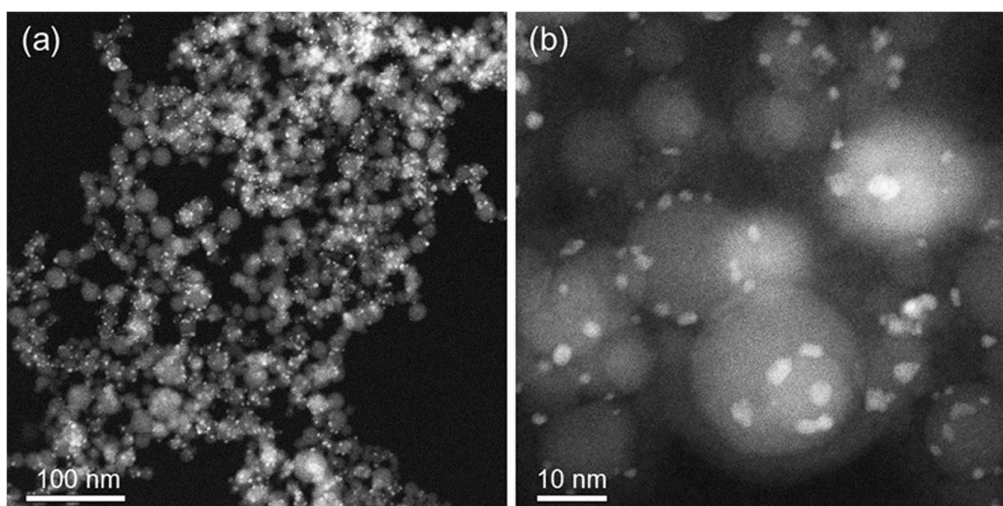


**Figure 2:** Low (a) and medium (b) magnification HAADF–STEM image of the as-synthesized Pd/Al<sub>2</sub>O<sub>3</sub> catalyst, respectively.

In addition to the XRD pattern, analysis by X-ray photoelectron spectroscopy (XPS) also reveals that the **Pd/Al<sub>2</sub>O<sub>3</sub> as-synthesized** material contains Pd catalyst particles in their terminal PdO oxidation state. This conclusion is supported directly by the observed binding energy (BE) of the Pd 3d<sub>5/2</sub> component at 336.9 eV (Figure 3, top) [44]. The as-synthesized nature of this PdO oxidation state is indicated by the minimal changes in the XPS signatures of Pd 3d and C 1s produced by intentionally oxidizing the as-synthesized sample (Figure 3, middle). In order to characterize the sample as it is used for the catalytic testing, XPS analysis was also performed after the reduction of the sample (**Pd/Al<sub>2</sub>O<sub>3</sub> reduced**). In contrast to the as-synthesized sample, under reducing conditions the dominant Pd 3d<sub>5/2</sub> component shifts to 335.3 eV (purple in Figure 3, bottom), i.e., into the BE range of 335.1–335.4 eV previously reported [44,45] for metallic Pd. Furthermore, the chemistry of the associated organic material (solid symbols in C 1s region, Figure 3) also undergoes an apparent reduction from oxidized to aliphatic (red and blue C 1s components in Figure 3, respectively) [25].

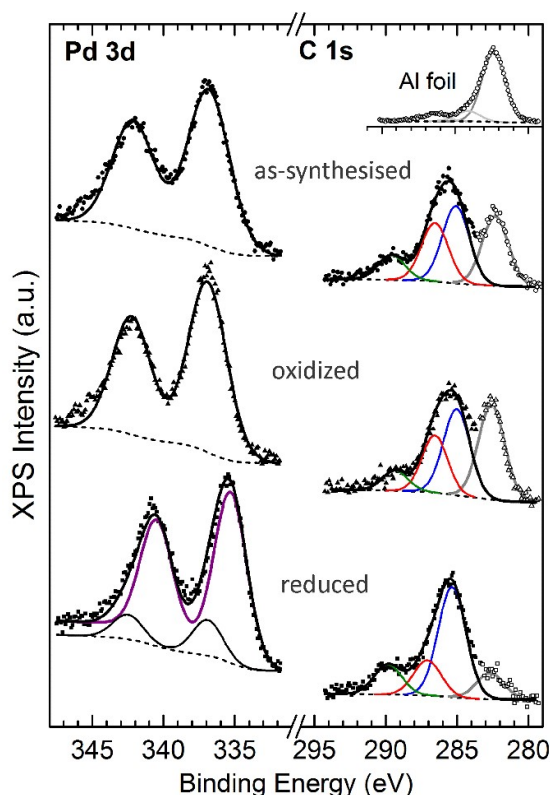


**Figure 3:** High-resolution XPS data for Pd 3d and C 1s regions. Supported-catalyst powders were measured as-synthesized (**Pd/Al<sub>2</sub>O<sub>3</sub> as-synthesized**) and after oxidation or reduction treatments (**Pd/Al<sub>2</sub>O<sub>3</sub> reduced**) (top-to-bottom). Differential charging produced a consistent 2.5 eV shift between aliphatic C 1s components corresponding to the supported-catalyst particles (blue lines, solid symbols) and Al-foil substrate (grey lines, open symbols, cf. top-right inset). Binding energy is presented after a correction (uniformly applied for all the catalyst samples), which placed the reference aliphatic C 1s peak (blue lines) at  $285.0 \pm 0.2$  eV. Symbols: raw data; thick lines: overall fits; thin colored lines: fits of individual components; dashed lines: background.

To characterize the active surface area of the catalyst, H<sub>2</sub> chemisorption was performed, on **Pd/Al<sub>2</sub>O<sub>3</sub> reduced**, and the results are summarized in Table 1. The average palladium particle size ( $d_M$ ) determined by hydrogen titration is approximately 6 nm, while the particle size determined by HAADF-STEM is 2.85 nm. The palladium dispersion ( $D_M$ ) is 19% and the metallic surface area ( $S_M$ ) is  $83 \text{ m}^2 \text{ g}^{-1}$ . The BET specific surface area ( $S_{\text{BET}}$ ), total pore volume ( $V_p$ ) and pore width ( $d_p$ ) of the **Pd/Al<sub>2</sub>O<sub>3</sub> as-synthesized** catalyst were determined by N<sub>2</sub> physisorption, and the results are summarized on Table 1. The sample presents a surface area of  $118 \text{ m}^2 \text{ g}_{\text{cat}}^{-1}$ , a total pore volume of  $0.3 \text{ cm}^3 \text{ g}_{\text{cat}}^{-1}$  and a pore width of 2 nm.

**Table 1:** Textural properties of the as-synthesized Pd/Al<sub>2</sub>O<sub>3</sub> sample.

	Amount of surface- bound H <sub>2</sub> <sup>a</sup> ( $\mu\text{mol g}_{\text{cat}}^{-1}$ )	$D_M$ <sup>a</sup> (%)	$S_M$ <sup>a</sup> ( $\text{m}^2 \text{g}_{\text{cat}}^{-1}$ )	$d_M$ <sup>a</sup> (nm)	$d_M$ <sup>b</sup> (nm)	$S_{\text{BET}}$ <sup>c</sup> ( $\text{m}^2 \text{g}_{\text{cat}}^{-1}$ )	$V_p$ <sup>c</sup> ( $\text{cm}^3 \text{g}_{\text{cat}}^{-1}$ )	$d_p$ <sup>c</sup> (nm)
Al <sub>2</sub> O <sub>3</sub>	—	—	—	—	—	108	0.4	2
Pd/Al <sub>2</sub> O <sub>3</sub>	43.5	19	83	6.2	2.85	118	0.3	2

<sup>a</sup> Determined by H<sub>2</sub> chemisorption<sup>b</sup> Determined by HAADF-STEM<sup>c</sup> Determined by N<sub>2</sub> physisorption

### 3.2 Catalytic measurements for acetylene semi-hydrogenation reaction

Figure 4 presents the catalytic measurements results, as a function of temperature and time on stream, of acetylene semi-hydrogenation reaction on **Pd/Al<sub>2</sub>O<sub>3</sub> reduced** and **Pd/Al<sub>2</sub>O<sub>3</sub>\_Ref reduced**, both reduced *in-situ*; in this sub-section, these samples will be denoted as **Pd/Al<sub>2</sub>O<sub>3</sub>** and **Pd/Al<sub>2</sub>O<sub>3</sub>\_Ref**, respectively. Figure 4a presents the Arrhenius plot of ethylene formation turnover frequency (TOF), from which the activation energy of acetylene hydrogenation is determined. Figure 4b shows the variation of acetylene conversion ( $X_{\text{C}_2\text{H}_2}$ ) and ethylene formation selectivity ( $S_{\text{C}_2\text{H}_4}$ ) with temperature for both samples tested and Figure 4c shows the same parameters as a function of time on stream.

Both samples display an increase in acetylene conversion and ethylene selectivity with temperature: In the case of the reference sample (**Pd/Al<sub>2</sub>O<sub>3</sub>\_Ref**),  $X_{\text{C}_2\text{H}_2}$  increases from 23% at 325 K to 92% at 500 K and  $S_{\text{C}_2\text{H}_4}$  increases from 34% at 325 K to 56% at 500 K. For **Pd/Al<sub>2</sub>O<sub>3</sub>**,  $X_{\text{C}_2\text{H}_2}$  increases from 12% at 325 K to 97% at 500 K and  $S_{\text{C}_2\text{H}_4}$  increases from 42% at 325 K to 62% at 470 K. **Pd/Al<sub>2</sub>O<sub>3</sub>** behaves similarly to the reference sample, with somewhat higher selectivity for ethylene formation, for the tested temperatures. Regarding the stability, evaluated with the variation of  $X_{\text{C}_2\text{H}_2}$  and  $S_{\text{C}_2\text{H}_4}$  over time (Figure 4c), both samples show similar  $X_{\text{C}_2\text{H}_2}$  values at 473 K over the tested time on stream, which decreases from 99% to 83% in the case of **Pd/Al<sub>2</sub>O<sub>3</sub>** and from 97% to 85% for **Pd/Al<sub>2</sub>O<sub>3</sub>\_Ref**, after 9 h. In terms of  $S_{\text{C}_2\text{H}_4}$ , the value remains constant over 9 h of time on stream for both samples, with **Pd/Al<sub>2</sub>O<sub>3</sub>** showing a higher selectivity ( $\approx 70\%$ ) than **Pd/Al<sub>2</sub>O<sub>3</sub>\_Ref** ( $\approx 60\%$ ).

The turnover frequency of ethylene formation was determined experimentally for the different temperatures tested and it increases with temperature, for both samples, reaching a value of 5 s<sup>-1</sup> and 3 s<sup>-1</sup> at 500 K for **Pd/Al<sub>2</sub>O<sub>3</sub>** and **Pd/Al<sub>2</sub>O<sub>3</sub>\_Ref**, respectively. From the Arrhenius plot (Figure 4a) it is possible to determine the activation energy ( $E_a$ ) for acetylene hydrogenation under the established conditions for the tested samples. Sample **Pd/Al<sub>2</sub>O<sub>3</sub>** exhibits an  $E_a$  of  $5.0 \pm 0.7 \text{ kcal mol}^{-1}$ , while **Pd/Al<sub>2</sub>O<sub>3</sub>\_Ref** exhibits an  $E_a$  of  $3.5 \pm 0.6 \text{ kcal mol}^{-1}$ .

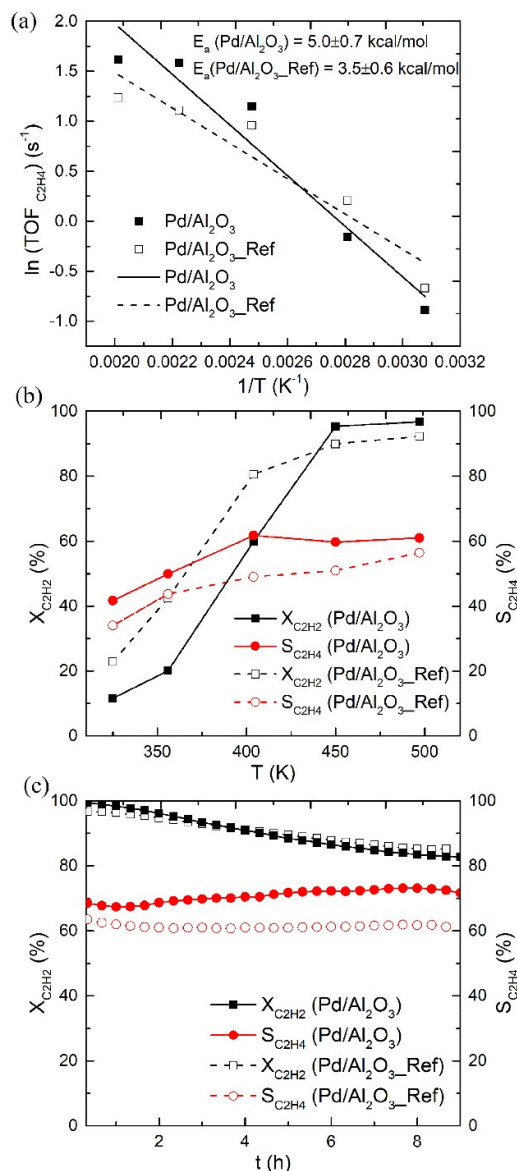


**Figure 4:** Catalytic measurement results as a function of the temperature and time on stream of acetylene semi-hydrogenation reaction on  $\text{Pd}/\text{Al}_2\text{O}_3$  and  $\text{Pd}/\text{Al}_2\text{O}_3\text{-Ref}$ . The Arrhenius plot of ethylene formation turnover frequency (TOF) (a); acetylene conversion ( $X_{\text{C}_2\text{H}_2}$ ) and ethylene formation selectivity ( $S_{\text{C}_2\text{H}_4}$ ), as a function of the temperature (b) and time on stream (c).

### 3.3 DFT simulations and microkinetic modelling

**3.3.1 Cluster-surface interaction.** Figure 5 gives the optimized model catalyst structure of  $\text{Pd}_{30}/\gamma\text{-Al}_2\text{O}_3(100)$ . Upon optimization, the  $\text{Pd}_{30}$  cluster still shows the pyramid-like structure with a base dimension of  $8.03 \times 7.95 \text{ \AA}^2$  and average height of  $5.78 \text{ \AA}$ . The optimized average Pd-Pd bond length is  $2.76 \text{ \AA}$ , slightly larger than the  $2.75 \text{ \AA}$  value in bulk Pd. The bond distances between the cluster base and support outermost layer vary in the range of  $2.13\text{--}2.23 \text{ \AA}$  (Pd-O).

The calculated cluster adsorption energy ( $E_{ads}^1$ ) of  $Pd_{30}$  is 12.46 eV (0.195 eV  $\text{\AA}^{-2}$ ). Here,  $E_{ads}^1$  is defined as

$$E_{ads}^1 = E(Pd_{30}) + E(Al_2O_3) - E(Pd_{30}/Al_2O_3) \quad (8)$$

where  $E(X)$  is the total energy of the related system  $X$ . The Bader charge analysis reveals that the  $Pd_{30}$  cluster gains  $1.64e$  of electron density in total, originating from the  $Al_2O_3$  substrate, which makes the negatively charged catalyst prone to attract reactant molecules.

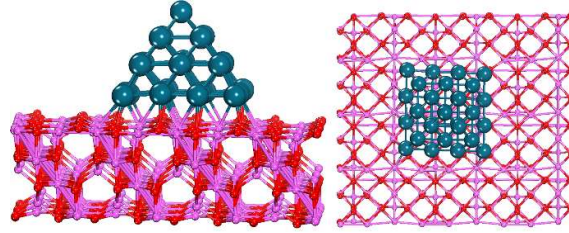


**Figure 5:** Model structure (side-view and top-view) of a pyramidal  $Pd_{30}$  cluster on  $\gamma$ - $Al_2O_3$  (100) surface. Color key: Pd, dark green; O, red; Al, pink.

The projected density of states (PDOS) of electronic structure, charge density difference (CDD), and HOMO–LUMO orbital distributions are displayed in Figure 6. PDOS (Figure 6a) shows the projection of Kohn-Sham single-particle states onto atomic s-, p- and d-components in the catalyst and support, respectively. At the Fermi energy, the weight of PDOS is significant on the cluster (Pd d-orbitals), while the support (insulator) exhibits a band-gap structure. In addition, the d-band center of  $Pd_{30}$  cluster, relative to the cluster Fermi energy, is calculated to be  $-2.00$  eV, close to the experimental d-band centers in extended (bulk) Pd surfaces of  $-2.02$  eV [46] and  $-2.09$  eV [47]. The CDD visualization (Figure 6b) displays a significant charge accumulation and depletion at the interface between the  $Pd_{30}$  cluster and  $Al_2O_3$  substrate, providing more insight for the observed charge transfer. In particular, the accumulated charge is distributed around the cluster perimeter. Furthermore, the HOMO and LUMO orbital distributions (Figure 6b) show that both states that are relevant to chemical reactivity are mainly delocalized within the  $Pd_{30}$  cluster, with very small weight on the  $Al_2O_3$  support.

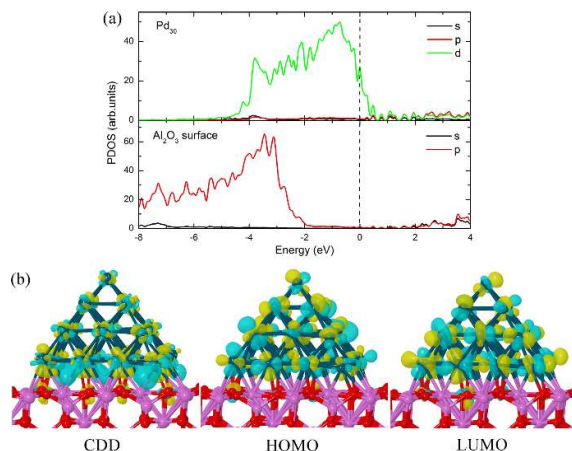


**Figure 6:** The electronic properties of  $\text{Pd}_{30}/\text{Al}_2\text{O}_3(100)$  system: (a) Projected density states (PDOS) on the atomic s-, p- and d- orbitals in the cluster and support, respectively. The vertical line indicates the Fermi level. (b) Side view of charge density difference (CDD) and HOMO–LUMO orbitals. The yellow and aqua colors for CDD represent charge depletion and accumulation, respectively. For HOMO/LUMO these colors represent the different signs of the wavefunction. The isosurface values are  $\pm 0.002 \text{ e a}_0^{-3}$  for CDD and  $\pm 0.01 \text{ e a}_0^{-3}$  for HOMO and LUMO.

**3.3.2 Acetylene hydrogenation.** The optimal adsorption site of the  $\text{H}_2$  molecule was mapped by testing  $\text{H}_2$  on different sites of the  $\text{Pd}_{30}$  cluster surface, and the results are presented in supplementary material. Figure 7 displays the structures of the initial state (IS), transition state (TS), intermediate state (IM), and final state (FS), and the energy diagrams along the hydrogenation pathways of acetylene to ethylene (Figure 7a) and consecutive unwanted ethylene to ethane (Figure 7b). At IS1,  $\text{C}_2\text{H}_2$  binds on the hollow site of the  $\text{Pd}_{30}$  surface with  $E_{ads}^2 = 2.11 \text{ eV}$ . The adsorbed  $\text{C}_2\text{H}_2$  molecule receives  $0.16e$  electron density from the catalyst. During the acetylene hydrogenation reaction,  $\text{C}_2\text{H}_2$  is first hydrogenated to  $\text{C}_2\text{H}_4$  by attaching two H atoms through TS1, IM1, and TS2 along the reaction pathway as shown in Figure 7a. In the first transition state (TS1), H atom moves to the adjacent Pd top site from its original hollow site with a H–Pd and H–C bond of 1.57 and 1.65 Å, respectively. At the same time, the orientation of  $\text{C}_2\text{H}_2$  also changes slightly, and the activation barrier is 0.72 eV (TS1). After this, the first intermediate state (IM1) of  $\text{C}_2\text{H}_3$  is formed with an exothermic energy of 0.05 eV. The activation barrier for the second H atom (TS2) is 0.75 eV with H–Pd and H–C bond lengths of 1.57 and 1.88 Å, respectively. The first product molecule of  $\text{C}_2\text{H}_4$  is formed in FS1 by the H atom binding to  $\text{C}_2\text{H}_3$  and the reaction energy is  $-0.36 \text{ eV}$ .

Following the first-step hydrogenation of  $\text{C}_2\text{H}_2$  to  $\text{C}_2\text{H}_4$ , two additional H atoms were placed on the same hollow sites of the  $\text{Pd}_{30}$  surface.  $\text{C}_2\text{H}_4$  prefers to bind on a bridge site of the  $\text{Pd}_{30}(\text{H})_2$  surface with the adsorption energy of 1.33 eV and a net charge of  $-0.05e$ . Next,  $\text{C}_2\text{H}_4$  is hydrogenated to the final product (FS2) of  $\text{C}_2\text{H}_6$  by attaching H atoms one-by-one. The reaction pathway in Figure 7b includes two transition states with activation barriers of 0.92 eV (TS3) and

0.81 eV (TS4) and one intermediate (IM2,  $C_2H_5$ ) with reaction energy of 0.26 eV. The corresponding higher activation barriers give the first indication for ethylene selectivity. The final product of  $C_2H_6$  (FS2) is generated with an exothermic energy of  $-0.10$  eV. The C–C and C–H bond lengths of the  $C_2H_6$  molecule are 1.53 and 1.10 Å (1.54 and 1.11 Å in gas-phase), respectively.

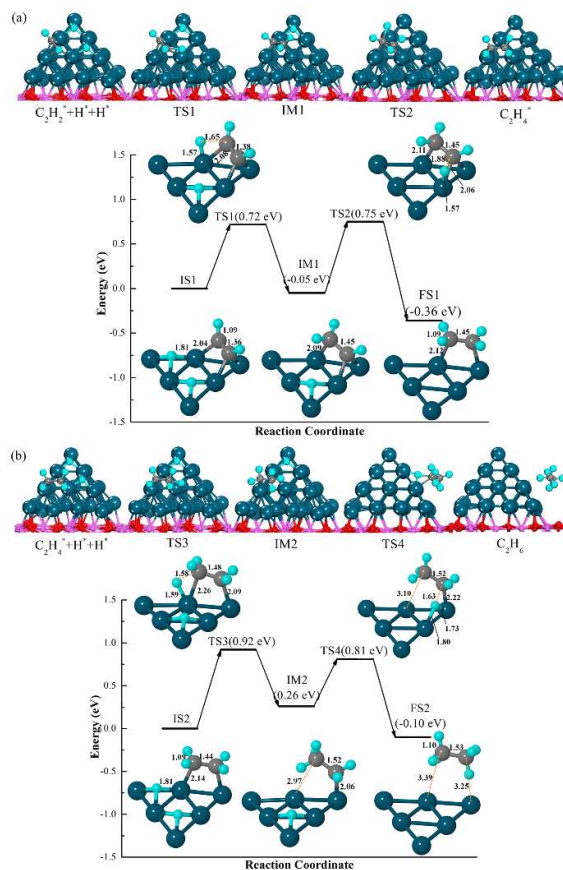


**Figure 7:** Structures of the initial state (IS), transition state (TS), intermediate state (IM), and final state (FS), and the energy diagrams along the hydrogenation pathways of (a) acetylene to ethylene ( $C_2H_2^* + H^* + H^* \rightarrow C_2H_4^*$ ), and (b) ethylene to ethane ( $C_2H_4 + H^* + H^* \rightarrow C_2H_6$ ) over  $Pd_{30}/Al_2O_3(100)$ . The energy diagrams display the reactants/products and a cluster (111)-facet (only fraction of the cluster). The geometrical parameters (in Å) are also given. The symbol \* refers to the atom or molecule being adsorbed on the catalyst. Color key: Pd, dark green; H, aqua; C, gray; O, red; Al, pink.

**3.3.3 Microkinetic simulations.** Figure 8 displays the microkinetic results for the temperature dependence of the Arrhenius plot of ethylene formation turnover frequency (TOF), acetylene conversion ( $X_{C_2H_2}$ ) and ethylene formation selectivity ( $S_{C_2H_4}$ ), and the surface coverages of hydrogen ( $\theta_H$ ), and acetylene ( $\theta_{C_2H_2}$ ). The simulations show that the TOFs of ethylene increase with temperature. The apparent activation energy ( $E_a$ ) of acetylene hydrogenation is  $8.8 \pm 0.6$  kcal mol $^{-1}$  by fitting the Arrhenius plot in Figure 8a. Here, we need to emphasize that this



apparent activation energy is different from the DFT-calculated activation barriers in the elementary reaction steps, as shown in Figure 7.

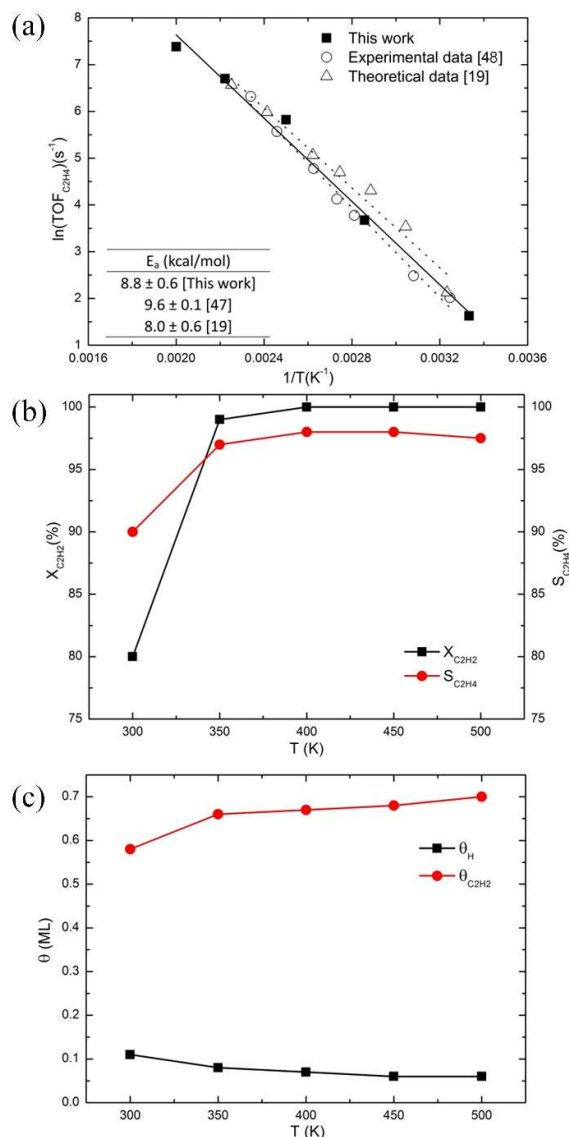


**Figure 8:** Microkinetic modeling results as a function of the temperature in acetylene hydrogenation over  $\text{Pd}_{30}/\text{Al}_2\text{O}_3(100)$ . (a) Arrhenius plot of ethylene formation turnover frequency (TOF), (b) Acetylene conversion ( $X_{\text{C}_2\text{H}_2}$ ) and ethylene formation selectivity ( $S_{\text{C}_2\text{H}_4}$ ), and (c) surface coverage of hydrogen ( $\theta_{\text{H}}$ ) and acetylene ( $\theta_{\text{C}_2\text{H}_2}$ ).

The simulated results of  $X_{\text{C}_2\text{H}_2}$  and  $S_{\text{C}_2\text{H}_4}$  as a function of temperature are plotted in Figure 8b. Both increase with the temperature between 300 and 500 K;  $X_{\text{C}_2\text{H}_2}$  increases from 80% at 300 K to 100% at 400 K, and  $S_{\text{C}_2\text{H}_4}$  increases from 90% at 300 K to 99% at 470 K. The formation of  $\text{C}_4$  and  $\text{C}_6$  byproducts are not included in the current simulations, which can lower the ethylene selectivity at the lower temperature [48].



The surface coverages of all species were also examined, and those for hydrogen ( $\theta_{\text{H}}$ ) and acetylene ( $\theta_{\text{C}_2\text{H}_2}$ ) are plotted as a function of temperature in Figure 8c. They exhibit opposite behavior with increasing temperature:  $\theta_{\text{H}}$  decreases from 0.11 ML at 300 K to 0.06 ML at 450 K, while  $\theta_{\text{C}_2\text{H}_2}$  increases from 0.58 ML at 300 K to 0.70 ML at 500 K. Furthermore, the surface coverages of vinyl, ethylene, and ethyl (not shown) are very low in the range of the temperatures considered herein.

#### 4. Discussion

Here, we present a combined approach using both experimental and theoretical studies to develop and validate a theoretical model for predicting behavior of catalysts. Typically, it is possible to find overlapping experimental and theoretical studies in the literature, however, combined approaches are rather rare. A Pd/Al<sub>2</sub>O<sub>3</sub> catalyst (**Pd/Al<sub>2</sub>O<sub>3</sub> as-synthesized**) was synthesized using the flame spray pyrolysis method, a typical method for catalyst preparation, and it was used as standard catalyst, after *in situ* reduction (**Pd/Al<sub>2</sub>O<sub>3</sub> reduced**), to test the theoretical model obtained through computational simulations. The performance of a representative Pd<sub>30</sub> cluster was simulated and it was compared with the real Pd catalyst on alumina to confirm the success of the developed model.

The characterization of the **Pd/Al<sub>2</sub>O<sub>3</sub> as-synthesized** sample by XRD showed that the Pd catalyst nanoparticles are in the PdO state (Figure 1), which is expected due to oxidation of the catalysts during synthesis because of high oxidation conditions present in the flame. This result was confirmed by XPS analysis with the binding energy (BE) of the Pd 3d<sub>5/2</sub> (Figure 3) which is in excellent agreement with the BE of 336.8 eV previously reported by Brun *et al.* [44] for a reference PdO powder. However, as shown from the XPS results, after reduction (**Pd/Al<sub>2</sub>O<sub>3</sub> reduced**), the dominant Pd 3d<sub>5/2</sub> component is in the range of 335.1–335.4 eV, previously reported [44,45] for metallic Pd, which means that the catalysts nanoparticles are metallic Pd after *in situ* reduction and before reaction. XPS confirms the reduction of the associated organic material from oxidized to aliphatic, thus, supporting the conclusion that both Pd and organic constituents of the sample become oxidized during synthesis rather than due to the subsequent exposure to air. We note that the 0.5–3 eV higher BE values reported for the metallic and oxidized Pd supported on insulating (e.g., alumina [49] or zeolite [50]) particles may result from the ambiguous nature of the C 1s component assigned as the aliphatic-carbon BE reference: The possible artifacts due to differential charging are highlighted by the 2.5 eV separation explicitly observed in this work between the spectral signatures derived from the Al-foil substrate and the supported catalyst particles (open and solid symbols in Figure 3, respectively).

The HAADF–STEM shows, as expected, that the catalyst prepared using flame spray pyrolysis (**Pd/Al<sub>2</sub>O<sub>3</sub> as-synthesized**) yielded spherical PdO particles with an average size of 2.85 nm

(Table 1), uniformly distributed on the supporting material (Figure 2). The obtained average size and particle shape is similar to those reported, for example, by Strobel *et al.* [51] for a Pd on alumina sample also prepared by FSP, which presents spherical shaped Pd nanoparticles with an average size of 2.7 nm. The structure and morphology of the support were maintained after the deposition of the Pd nanoparticles (Table 1). The specific surface area ( $S_{\text{BET}}$ ), pore volume ( $V_p$ ) and pore diameter ( $d_p$ ) are similar for the used  $\text{Al}_2\text{O}_3$  support and for the **Pd/ $\text{Al}_2\text{O}_3$  as-synthesized** catalyst, which confirms that the deposition of the Pd nanoparticles did not alter the microstructure of the support. Similarly to the Pd particle size, the microstructure of our sample is comparable to the properties of the catalyst prepared by Strobel *et al.* [51], which had a specific surface area of  $120 \text{ m}^2 \text{ g}_{\text{cat}}^{-1}$ .

The particle sizes were determined both by HAADF–STEM, on the **Pd/ $\text{Al}_2\text{O}_3$  as-synthesized sample**, and  $\text{H}_2$  chemisorption on the **Pd/ $\text{Al}_2\text{O}_3$  reduced** catalyst (Table 1): the particle size obtained from  $\text{H}_2$  chemisorption is higher. This discrepancy is due to the different weighting of the two procedures: chemisorption determines the surface-area weighted diameter, while HAADF–STEM determines the number-average diameter. Importantly, the value determined by chemisorption provides valuable information for heterogeneous catalysis, as it is related to the active metallic surface area. The values of Pd dispersion and particle size obtained by  $\text{H}_2$  chemisorption (Table 1) are comparable to those obtained by Strobel *et al.* [51] using CO chemisorption.

The results obtained for the conversion and selectivity of the **Pd/ $\text{Al}_2\text{O}_3$  reduced** and **Pd/ $\text{Al}_2\text{O}_3$ \_Ref reduced** samples (Figure 4) are similar, which confirms that **Pd/ $\text{Al}_2\text{O}_3$  reduced** can be used as a model catalyst since it behaves similarly to the commercial reference sample. In addition, the obtained results agree with those found in the literature [12,48] in the range of the tested temperatures. In this work, to simplify the theoretical simulations, a simplified gas mixture was used, neglecting the large excess of ethylene common in the industrially relevant feed composition (non-competitive conditions). Thus, the results were compared to studies where the excess of ethylene was also omitted. Table 2 presents a comparison of the experimental results obtained in this work with those reported in the literature for similar catalysts.

**Table 2:** Comparison of catalyst performance, determined experimentally (Exp) and theoretically (Theo).

Catalyst	$X_{\text{C}_2\text{H}_2}$ (%) at 450K	$S_{\text{C}_2\text{H}_4}$ (%) at 450K	$E_a$ ( $\text{kcal mol}^{-1}$ )	$m_{\text{cat}}$ (mg)	Feed Composition ( $\text{C}_2\text{H}_2:\text{H}_2$ )	Ref.
<b>Pd/<math>\text{Al}_2\text{O}_3</math></b>	80	75	–	0.5	1:2	Exp [12]
<b>Pd foil</b>	–	94 <sup>1</sup>	9.6±0.1	–	1:1	Exp [48]
<b>Pd (111)</b>	–	95	8.0±0.6	–	1:1	Theo [19]

<sup>1</sup> Determined for conversions <1%

<b>Pd/Al<sub>2</sub>O<sub>3</sub></b>	95	60	5.0±0.7	1	1:10	Exp	This work
<b>Pd/Al<sub>2</sub>O<sub>3</sub>_Ref</b>	90	51	3.5±0.6	1	1:10	Exp	This work
<b>Pd<sub>30</sub>/Al<sub>2</sub>O<sub>3</sub></b>	100	98	8.8±0.6	—	1:10	Theo	This work

Osswald *et al.* [12] tested a Pd on Al<sub>2</sub>O<sub>3</sub> reference catalyst which achieved a maximum conversion at 450 K, and a similar temperature dependence of activity was observed in the current work (Figure 4). The activity reported by Osswald *et al.* at 450 K is lower ( $\approx 80\%$ ) than that obtained for both samples here (95% and 90%). The catalysts studied by Osswald *et al.* exhibit higher selectivity in the 350–500 K interval, ranging from 60% to 80% [12]. Molero *et al.* [48], tested a palladium foil sample for acetylene semi-hydrogenation where the selectivity increased drastically from approximately 30% at 300 K to 94% at 470 K. Considering the selectivity and conversion results, the sample prepared and tested in this study exhibits an overall trend similar to the results found in the literature, however, with slightly different selectivity [12,48]. We note that these differences in the selectivity and conversion values can be due to differences in the experimental conditions, i.e., different feed composition and mass of catalyst used. Osswald *et al.* [12] used a feed composition of 2% acetylene and 4% hydrogen in helium and 0.5 mg of catalyst, while Molero *et al.* [48] performed the reaction with a ratio of acetylene to hydrogen of 1:1.

In terms of stability, the selectivity values in Figure 4c agree with previous studies [12], but the conversion rate has a smaller decrease compared to the study of Osswald *et al.* [12], where the stability of a reference Pd on alumina catalyst was also tested and the conversion decreased from 100% to around 20% after 9 h, while the selectivity was approximately stable at 60% [12]. As above, we note that the reaction conditions used in Ref [12] are different from ours.

Our computational studies suggest a comparable catalytic activity for acetylene hydrogenation on a Pd<sub>30</sub> cluster and on Pd surfaces, as expected based on the similar d-band centers of these systems (Figure 6a). However, the microkinetic simulations (Figure 8) predict a higher activity and selectivity for the Pd<sub>30</sub> clusters, and the predicted trends agree with those obtained in the experimental results (Figure 4). The selectivity for ethylene determined in the microkinetic simulations agrees well with the previous results for simulations [19] and experiments for surfaces [48] in the same range of temperatures. The quantitative differences between the experiments (Pd/Al<sub>2</sub>O<sub>3</sub>) and theory (Pd<sub>30</sub>/Al<sub>2</sub>O<sub>3</sub>(100)) can be explained by the particle size: the clusters in Pd<sub>30</sub>/Al<sub>2</sub>O<sub>3</sub>(100) are considerably smaller than the Pd nanoparticles on Pd/Al<sub>2</sub>O<sub>3</sub>, which explains the lower experimental selectivity. The larger Pd nanoparticles favor the formation of the  $\beta$ -hydride phase, which supplies active hydride species to surfaces resulting in full hydrogenation of acetylene to ethane, thus decreasing the ethylene selectivity [52,53]. Furthermore, our microkinetic model has been parameterized at low coverage limit which may affect the results.

The computed activation energy over Pd<sub>30</sub>/Al<sub>2</sub>O<sub>3</sub>(100) ( $8.8 \pm 0.6$  kcal mol<sup>-1</sup>) is comparable to the experimental value obtained by Molero *et al.* [48], of  $9.6 \pm 0.1$  kcal mol<sup>-1</sup> over a clean Pd foil,

and with the computed by Mei *et al.* [19] value, of  $8.0 \pm 0.6$  kcal mol<sup>-1</sup> over Pd(111), at the conditions of  $P(\text{H}_2) = P(\text{C}_2\text{H}_2) = 100$  Torr and the temperature range of 300–500 K, but the activation energy obtained experimentally for the **Pd/Al<sub>2</sub>O<sub>3</sub> reduced** sample is slightly lower ( $5.0 \pm 0.7$  kcal mol<sup>-1</sup>). Again, these values are sensitive to the experimental conditions (feed composition), catalyst itself (film, nanoparticle), as well as synthetic history.

Figure 9 shows the comparison between the acetylene conversion ( $X_{\text{C}_2\text{H}_2}$ ) and ethylene formation selectivity ( $S_{\text{C}_2\text{H}_4}$ ) results, as a function of the temperature, determined experimentally and theoretically. It can be observed that the results obtained experimentally with the **Pd/Al<sub>2</sub>O<sub>3</sub> reduced** catalyst qualitatively agree with the microkinetic simulations based on parameters from extensive DFT calculations over a **Pd<sub>30</sub>/Al<sub>2</sub>O<sub>3</sub>(100)** model catalyst. The predicted and experimental conversions agree well at temperatures above 450 K, while selectivities and conversions at lower temperatures are different, apart from the agreement in the general trend of increasing of activity and selectivity with temperature. In addition to the aforementioned reasons, the mismatch between theory and experiment may be due to simplifications used in the modeling where the dissolution of hydrogen and carbon in the Pd subsurface region were not considered [52]. More expensive calculations where the structure of Pd cluster is flexible and can be refined are required to improve the theoretical results. Nevertheless, the good agreement at high temperatures show that the model used in this study can be used for fast screening of potential catalysts, especially of intermetallic catalysts with covalent bonding where the dissolution of hydrogen or carbon is suppressed [24]. Conversely, the high selectivity predicted by the theory indicates that novel material designs that attempt to minimize the dissolution of hydrogen and carbon in Pd should be considered for increasing the selectivity of the practical catalysts.

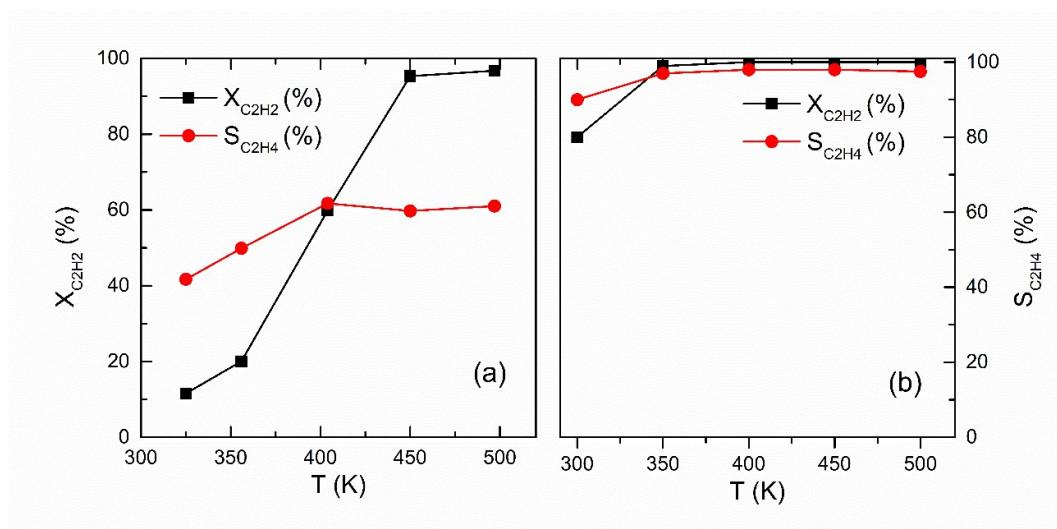


**Figure 9:** Acetylene conversion ( $X_{C_2H_2}$ ) and ethylene formation selectivity ( $S_{C_2H_4}$ ), as a function of the temperature, determined experimentally (a) and theoretically (b).

## 5. Conclusions

It has been shown that by high-throughput FSP method it is possible to prepare large quantities of active and selective Pd catalyst for the acetylene semi-hydrogenation reaction. In particular, the prepared catalyst, reduced *in situ*, achieves a conversion of acetylene of 97% at 500 K and a selectivity to ethylene of 62% at 470 K. Furthermore, these results correlate with the microkinetic simulations based on parameters from extensive DFT calculations over a  $Pd_{30}/Al_2O_3(100)$  model catalyst. The insights gained from this direct comparison can be applied to a parallel computational screening of complex hydrogenation catalysts and synthesis and investigation of the most promising candidates, in the context of both the industrial polymerization process and the novel applications in the  $H_2$  economy.

## Conflicts of interest

There are no conflicts to declare.

## Acknowledgements

This work was supported by the European Union's Horizon 2020 research and innovation program through the CritCat Project under Grant Agreement No. 686053. L.P.L.G. is thankful for the support to FCT PhD grant SFRH/BD/128986/2017. This work is also a result of: Project "AIProcMat@N2020 - Advanced Industrial Processes and Materials for a Sustainable Northern Region of Portugal 2020", with the reference NORTE-01-0145-FEDER-000006, supported by Norte Portugal Regional Operational Programme (NORTE 2020), under the Portugal 2020 Partnership Agreement, through the European Regional Development Fund (ERDF); Associate

Laboratory LSRE-LCM – UID/EQU/50020/2019 – funded by national funds through FCT/MCTES (PIDDAC).

## Appendix A

Supplementary material: Supplementary data associated with this article can be found, in the online version.

## References

- [1] Borodziński A, Bond GC. Selective hydrogenation of ethyne in ethene-rich streams on palladium catalysts. Part 1. Effect of changes to the catalyst during reaction. *Catal Rev - Sci Eng* 2006;48:91–144. doi:10.1080/01614940500364909.
- [2] Spanjers CS, Held JT, Jones MJ, Stanley DD, Sim RS, Janik MJ, et al. Zinc inclusion to heterogeneous nickel catalysts reduces oligomerization during the semi-hydrogenation of acetylene. *J Catal* 2014;316:164–73. doi:10.1016/j.jcat.2014.05.007.
- [3] Trimm DL, Liu IOY, Cant NW. The selective hydrogenation of acetylene over a Ni/SiO<sub>2</sub> catalyst in the presence and absence of carbon monoxide. *Appl Catal A Gen* 2010;374:58–64. doi:10.1016/j.apcata.2009.11.030.
- [4] Guzzi L, Molnár Á, Teschner D. *Hydrogenation Reactions: Concepts and Practice*. vol. 7. Elsevier Ltd.; 2013. doi:10.1016/B978-0-08-097774-4.00713-0.
- [5] Okada Y, Sasaki E, Watanabe E, Hyodo S, Nishijima H. Development of dehydrogenation catalyst for hydrogen generation in organic chemical hydride method. *Int J Hydrogen Energy* 2006;31:1348–56. doi:10.1016/j.ijhydene.2005.11.014.
- [6] Guo Z, Liu Y, Liu Y, Chu W. Promising SiC support for Pd catalyst in selective hydrogenation of acetylene to ethylene. *Appl Surf Sci* 2018;442:736–41. doi:10.1016/j.apsusc.2018.02.145.
- [7] Kim SK, Kim C, Lee JH, Kim J, Lee H, Moon SH. Performance of shape-controlled Pd nanoparticles in the selective hydrogenation of acetylene. *J Catal* 2013;306:146–54. doi:10.1016/j.jcat.2013.06.018.
- [8] Benavidez AD, Burton PD, Nogales JL, Jenkins AR, Ivanov SA, Miller JT, et al. Improved selectivity of carbon-supported palladium catalysts for the hydrogenation of acetylene in excess ethylene. *Appl Catal A Gen* 2014;482:108–15. doi:10.1016/j.apcata.2014.05.027.

- [9] Molnár Á, Sárkány A, Varga M. Hydrogenation of carbon-carbon multiple bonds: Chemo-, regio- and stereo-selectivity. *J Mol Catal A Chem* 2001;173:185–221. doi:10.1016/S1381-1169(01)00150-9.
- [10] Zhang Q, Li J, Liu X, Zhu Q. Synergetic effect of Pd and Ag dispersed on Al<sub>2</sub>O<sub>3</sub> in the selective hydrogenation of acetylene. *Appl Catal A Gen* 2000;197:221–8. doi:10.1016/S0926-860X(99)00463-9.
- [11] Osswald J, Giedigkeit R, Jentoft RE, Armbrüster M, Girsdsies F, Kovnir K, et al. Palladium-gallium intermetallic compounds for the selective hydrogenation of acetylene. Part I: Preparation and structural investigation under reaction conditions. *J Catal* 2008;258:210–8. doi:10.1016/j.jcat.2008.06.013.
- [12] Osswald J, Kovnir K, Armbrüster M, Giedigkeit R, Jentoft RE, Wild U, et al. Palladium-gallium intermetallic compounds for the selective hydrogenation of acetylene. Part II: Surface characterization and catalytic performance. *J Catal* 2008;258:219–27. doi:10.1016/j.jcat.2008.06.014.
- [13] Han Y, Peng D, Xu Z, Wan H, Zheng S, Zhu D. TiO<sub>2</sub> supported Pd@Ag as highly selective catalysts for hydrogenation of acetylene in excess ethylene. *Chem Commun* 2013;49:8350. doi:10.1039/c3cc43511c.
- [14] Pei GX, Liu XY, Wang A, Lee AF, Isaacs MA, Li L, et al. Ag alloyed Pd single-atom catalysts for efficient selective hydrogenation of acetylene to ethylene in excess ethylene. *ACS Catal* 2015;5:3717–25. doi:10.1021/acscatal.5b00700.
- [15] Kim E, Shin EW, Bark CW, Chang I, Yoon WJ, Kim WJ. Pd catalyst promoted by two metal oxides with different reducibilities: Properties and performance in the selective hydrogenation of acetylene. *Appl Catal A Gen* 2014;471:80–3. doi:10.1016/j.apcata.2013.11.036.
- [16] Sárkány A, Weiss AH, Gucci L. Structure sensitivity of acetylene-ethylene hydrogenation over Pd catalysts. *J Catal* 1986;98:550–3. doi:10.1016/0021-9517(86)90343-X.
- [17] Crespo-Quesada M, Yarulin A, Jin M, Xia Y, Kiwi-Minsker L. Structure sensitivity of alkynol hydrogenation on shape- and size-controlled palladium nanocrystals: Which sites are most active and selective? *J Am Chem Soc* 2011;133:12787–94. doi:10.1021/ja204557m.

- [18] Sheth PA, Neurock M, Smith CM. A First-Principles Analysis of Acetylene Hydrogenation over Pd (111). *J Phys Chem B* 2003;2009–17. doi:10.1021/jp021342p.
- [19] Mei D, Sheth PA, Neurock M, Smith CM. First-principles-based kinetic Monte Carlo simulation of the selective hydrogenation of acetylene over Pd (111). *J Catal* 2006;242:1–15. doi:10.1016/j.jcat.2006.05.009.
- [20] Ma L, Lv C, Wang G. A DFT study and micro-kinetic analysis of acetylene selective hydrogenation on Pd-doped Cu (111) surfaces. *Appl Surf Sci* 2017;410:154–65. doi:10.1016/j.apsusc.2017.01.084.
- [21] Yang J, Lv CQ, Guo Y, Wang GC. A DFT+U study of acetylene selective hydrogenation on oxygen defective anatase (101) and rutile (110) TiO<sub>2</sub> supported Pd<sub>4</sub> cluster. *J Chem Phys* 2012;136:104107. doi:10.1063/1.3692292.
- [22] Meng LD, Wang GC. A DFT + U study of acetylene selective hydrogenation over anatase supported PdAg<sub>4</sub>(a + b = 4) cluster. *Phys Chem Chem Phys* 2014;16:17541–50. doi:10.1039/c4cp01818d.
- [23] Mädler L, Kammler HK, Mueller R, Pratsinis SE. Controlled synthesis of nanostructured particles by flame spray pyrolysis. *J Aerosol Sci* 2002;33:369–89. doi:10.1016/S0021-8502(01)00159-8.
- [24] Kovnir K, Armbrüster M, Teschner D, Venkov T V., Szentmiklósi L, Jentoft FC, et al. In situ surface characterization of the intermetallic compound PdGa - A highly selective hydrogenation catalyst. *Surf Sci* 2009;603:1784–92. doi:10.1016/j.susc.2008.09.058.
- [25] Lock EH, Petrovykh DY, Mack P, Carney T, White RG, Walton SG, et al. Surface Composition, Chemistry, and Structure of Polystyrene Modified by Electron-Beam-Generated Plasma. *Langmuir* 2010;26:8857–68. doi:10.1021/la9046337.
- [26] Stine R, Petrovykh DY. Oriented self-assembled monolayers of bifunctional molecules on InAs. *J Electron Spectrosc Relat Phenomena* 2009;172:42–6. doi:10.1016/j.elspec.2009.02.001.
- [27] Petrovykh DY, Smith JC, Clark TD, Stine R, Baker LA, Whitman LJ. Self-Assembled Monolayers of Alkanethiols on InAs. *Langmuir* 2009;25:12185–94. doi:10.1021/la804314j.
- [28] Li Y, Jang BW-L. Selective Hydrogenation of Acetylene Over Pd/Al<sub>2</sub>O<sub>3</sub> Catalysts:



Effect of Non-thermal RF Plasma Preparation Methodologies. *Top Catal* 2017;60:997–1008. doi:10.1007/s11244-017-0765-5.

- [29] CP2K n.d. <http://www.cp2k.org> (accessed November 3, 2017).
- [30] VandeVondele J, Krack M, Mohamed F, Parrinello M, Chassaing T, Hutter J. QUICKSTEP : Fast and accurate density functional calculations using a mixed Gaussian and plane waves approach 2005;167:103–28. doi:10.1016/j.cpc.2004.12.014.
- [31] Perdew JP, Burke K, Ernzerhof M. Generalized Gradient Approximation Made Simple. *Phys Rev Lett* 1996;77:3865–8. doi:10.1103/PhysRevLett.77.3865.
- [32] Goedecker S, Teter M, Hutter J. Separable dual-space Gaussian pseudopotentials. *Phys Rev B* 1996;54:1703–10. doi:10.1103/PhysRevB.54.1703.
- [33] Vandevondele J, Hutter J. Gaussian basis sets for accurate calculations on molecular systems in gas and condensed phases. *J Chem Phys* 2007;127:114105. doi:10.1063/1.2770708.
- [34] Lippert G, Hutter J, Parrinello M. A hybrid Gaussian and plane wave density functional scheme. *Mol Phys* 1997;92:477–87. doi:10.1080/002689797170220.
- [35] Grimme S, Antony J, Ehrlich S, Krieg H. A consistent and accurate ab initio parametrization of density functional dispersion correction ( DFT-D ) for the 94 elements H-Pu. *J Chem Phys* 2010;132:154104. doi:10.1063/1.3382344.
- [36] Tang W, Sanville E, Henkelman G. A grid-based Bader analysis algorithm without lattice bias. *J Phys Condens Matter* 2009;21:084204. doi:10.1088/0953-8984/21/8/084204.
- [37] Bader RFW. A quantum theory of molecular structure and its applications. *Chem Rev* 1991;91:893–928. doi:10.1021/cr00005a013.
- [38] Henkelman G, Uberuaga BP, Jónsson H. A climbing image nudged elastic band method for finding saddle points and minimum energy paths A climbing image nudged elastic band method for finding saddle points and minimum energy paths. *J Chem Phys* 2016;143:094105. doi:10.1063/1.4999947.
- [39] Digne M, Sautet P, Raybaud P, Euzen P, Toulhoat H. Use of DFT to achieve a rational understanding of acid – basic properties of  $\gamma$  -alumina surfaces. *J Catal* 2004;226:54–68. doi:10.1016/j.jcat.2004.04.020.

- [40] Honkanen M, Wang J, Kärkkäinen M, Huuhtanen M, Jiang H, Kallinen K, et al. Regeneration of sulfur-poisoned Pd-based catalyst for natural gas oxidation. *J Catal* 2018;358:253–65. doi:10.1016/j.jcat.2017.12.021.
- [41] Ma L, Melander M, Weckman T, Lipasti S, Laasonen K, Akola J. DFT simulations and microkinetic modelling of 1-pentyne hydrogenation on Cu<sub>20</sub> model catalysts. *J Mol Graph Model* 2016;65:61–70. doi:10.1016/j.jmgm.2016.02.007.
- [42] Ma L, Melander M, Weckman T, Laasonen K, Akola J. CO Oxidation on the Au<sub>15</sub>Cu<sub>15</sub> Cluster and the Role of Vacancies in the MgO (100) Support. *J Phys Chem C* 2016;120:26747–58. doi:10.1021/acs.jpcc.6b06876.
- [43] Ma L, Laasonen K, Akola J. Catalytic Activity of AuCu Clusters on MgO (100): Effect of Alloy Composition for CO Oxidation. *J Phys Chem C* 2017;121:10876–86. doi:10.1021/acs.jpcc.6b12054.
- [44] Brun M, Berthet A, Bertolini JC. XPS, AES and Auger parameter of Pd and PdO. *J Electron Spectros Relat Phenomena* 1999;104:55–60. doi:10.1016/S0368-2048(98)00312-0.
- [45] Powell CJ. Recommended Auger parameters for 42 elemental solids. *J Electron Spectros Relat Phenomena* 2012;185:1–3. doi:10.1016/j.elspec.2011.12.001.
- [46] Gorzkowski MT, Lewera A. Probing the Limits of d - Band Center Theory: Electronic and Electrocatalytic Properties of Pd-Shell – Pt-Core Nanoparticles. *J Phys Chem C* 2015;119:18389–95. doi:10.1021/acs.jpcc.5b05302.
- [47] Hofmann T, Yu TH, Folse M, Weinhardt L, Ba M, Zhang Y, et al. Using Photoelectron Spectroscopy and Quantum Mechanics to Determine d - Band Energies of Metals for Catalytic Applications. *J Phys Chem C* 2012;116:24016–26. doi:10.1021/jp303276z.
- [48] Molero H, Bartlett BF, Tysoe WT. The Hydrogenation of Acetylene Catalyzed by Palladium : Hydrogen Pressure Dependence. *J Catal* 1999;181:49–56. doi:10.1006/jcat.1998.2294.
- [49] Babu NS, Lingaiah N, Gopinath R, Sankar Reddy PS, Sai Prasad PS. Characterization and Reactivity of Alumina-Supported Pd Catalysts for the Room-Temperature Hydrodechlorination of Chlorobenzene. *J Phys Chem C* 2007;111:6447–53. doi:10.1021/jp065866r.

- [50] Mandal S, Roy D, Chaudhari R V, Sastry M. Pt and Pd Nanoparticles Immobilized on Amine-Functionalized Zeolite: Excellent Catalysts for Hydrogenation and Heck Reactions. *Chem Mater* 2004;16:3714–24. doi:10.1021/cm0352504.
- [51] Strobel R, Krumeich F, Stark WJ, Pratsinis SE, Baiker A. Flame spray synthesis of Pd/Al<sub>2</sub>O<sub>3</sub> catalysts and their behavior in enantioselective hydrogenation. *J Catal* 2004;222:307–14. doi:10.1016/j.jcat.2003.10.012.
- [52] Gigola CE, Aduriz HR, Bodnariuk P. Particle size effect in the hydrogenation of acetylene under industrial conditions. *Appl Catal* 1986;27:133–44. doi:10.1016/S0166-9834(00)81052-0.
- [53] Teschner D, Borsodi J, Wootsch A, Révay Z, Hävecker M. The Roles of Subsurface Carbon and Hydrogen in Palladium-Catalyzed Alkyne Hydrogenation. *Science* (80- ) 2008;320:86–90. doi:10.1126/science.1155200.